Electrochimica Acta 115 (2014) 131–139

Contents lists available at ScienceDirect

Electrochimica Acta

journal homepage: www.elsevier.com/locate/electacta

Three-dimensional electrochemical Li-ion battery modelling featuring a focused ion-beam/scanning electron microscopy based three-phase reconstruction of a $LiCoO_2$ cathode

T. Hutzenlaub[a,*,1], S. Thiele[b], N. Paust[a], R. Spotnitz[c,1], R. Zengerle[a,b], C. Walchshofer[d,1]

[a] HSG-IMIT—Institut für Mikro- und Informationstechnik, Georges-Koehler-Allee 103, 79110 Freiburg, Germany
[b] Laboratory for MEMS Applications, IMTEK—Department of Microsystems Engineering, University of Freiburg, Georges-Koehler-Allee 103, 79110 Freiburg, Germany
[c] Battery Design LLC, 2277 Delucchi Drive, Pleasanton, CA 94588, United States
[d] CD-adapco, Nürnberg office, Nordostpark 3-5, 90411 Nürnberg, Germany

ARTICLE INFO

Article history:
Received 8 August 2013
Received in revised form 14 October 2013
Accepted 18 October 2013
Available online 1 November 2013

Keywords:
Three-phase three-dimensional reconstruction
Li-ion battery cathode
Porous media
Microstructural electrochemical battery model
Pseudo-two-dimensional porous electrode model

ABSTRACT

We combine a three-phase, three-dimensional reconstruction of a $LiCoO_2$ battery cathode based on focused ion-beam/scanning electron microscopy (FIB/SEM) imaging with an electrochemical model. The model considers the electric potential and lithium/salt concentration distribution in both the liquid electrolyte and the solid active-material phases. In contrast to previously presented models, we spatially resolve the carbon-binder phase to provide a more realistic description of the electric potential. We observe that carbon-binder coverage of the solid electrolyte interface (SEI) impedes local surface reactions and thus affects lithium redistribution. For the considered cathode, the total surface to volume ratio of the SEI is reduced from 11.2×10^5 to 6.5×10^5 $m^2\ m^{-3}$ when the carbon-binder phase is modelled explicitly. This leads to increased inhomogeneity of the lithium concentration in active-material grains during charging.

Additionally, we study lithium/salt concentration in the electrolyte, revealing gradients between 0.9 and 1.5 kmol m^{-3} depending on the distance to the separator. This is significant because the lithium/salt concentration directly affects the ion transport properties of the electrolyte.

1. Introduction

Electrochemical engineering models at various levels of complexity are a well-established tool to predict and optimize Li-ion battery performance [1]. Simpler models such as the single-particle model [2–4], where the anode and cathode are each depicted by a particle with the same surface area as the real electrode, have the advantage of fast solution times. Their disadvantage is that they are valid only for very specific conditions such as low applied current densities and thin, highly conductive electrodes [4]. The most commonly used model is the so-called pseudo-two-dimensional (P2D) porous electrode model [5–14]. It accounts for electric potential and lithium/salt concentration over the cross-sectional area of a battery consisting of porous electrodes, separator and current collectors by solving coupled nonlinear partial differential equations. In recent years, mainly due to advances in available computational power, these models have been extended to include additional effects such as thermal–electrochemical coupling [15]. This increases complexity but also enables a more realistic representation of experiments. In reality, porous electrodes of a Li-ion battery do not consist of uniformly sized particles [16]. Consequently, there have been efforts to create more realistic geometrical representations: The Kinetic Monte Carlo simulation approach was used to model SEI heterogeneity [17]. Some extended models now include statistically created three-dimensionally resolved geometrical configurations [18,19] or describe the electrodes by a particle distribution [20–23].

Electrode morphology can be studied experimentally by employing focused ion-beam/scanning electron microscopy (FIB/SEM) [24]. The structure of a porous medium is investigated by repeatedly removing thin layers of material and imaging between ablation steps. A subsequent segmentation identifies the phases in each image. Finally, the images are arranged according to sequence with a displacement between neighbouring images equivalent to the slice thickness. This creates a three-dimensional representation of the porous medium which can be used for parameter extraction [25] and further modelling steps [26]. In the energy application sector, this method was applied to solid oxide fuel cells [27] and PEM fuel cells [28,29], and was subsequently also extended to Li-ion batteries [16,30–32].

* Corresponding author. Tel.: +49 761 203 73269; fax: +49 761 203 73299.
E-mail address: tobias.hutzenlaub@hsg-imit.de (T. Hutzenlaub).
[1] ISE member

0013-4686/$ – see front matter © 2013 Elsevier Ltd. All rights reserved.
http://dx.doi.org/10.1016/j.electacta.2013.10.103

c_0	concentration of the solvent 1 kmol m^{-3}(assumed)
c_{am}	molar concentration of lithium in active material (kmol m^{-3})
$c_{am,max}$	molar concentration of lithium in saturated electrode material anode: 2600.4 kmol m^{-3} [40] cathode: 51.555 kmol m^{-3} [40]
c_e	molar concentration of lithium cations in electrolyte (kmol m^{-3})
$c_{e,ref}$	molar reference concentration of lithium/salt in the electrolyte 1 kmol m^{-3}[40]
C	specific double-layer capacitance of the SEI anode: 0 A s V^{-1} m^{-2} [40] cathode: 0 A s V^{-1} m^{-2} [40]
D	lithium diffusivity anode: 10^{-13} m^2 s^{-1} (minimal resistance to transport of charge carriers assumed) active material: 10^{-14} m^2 s^{-1} [43]
D_0	reference lithium diffusivity (m^2 s^{-1}) (Table 1)
$\frac{d(\ln C_0)}{d(\ln C_e)}$	concentrated solution correction to salt diffusivity (−) (Table 1)
$\frac{d(\ln f+)}{d(\ln C_e)}$	non-ideal solution correction to salt migration (−) (Table 1)
$\vec{E}$	electric field (V m^{-1})
E_a	kinetic activation energy 0 J kmol^{-1} [40]
E_{SEI}	SEI activation energy 0 J kmol^{-1} [40]
F	Faraday's constant 96485342 A s kmol^{-1}
$f_\pm$	mean molar activity coefficient of the electrolyte (−)
$\vec{\tau}$	electric current density (A m^{-2})
$\vec{\tau}_{am}$	electric current density in the active-material phase (A m^{-2})
$\vec{\tau}_s$	electric current density in the electrolyte phase (A m^{-2})
i_0	exchange current density (A m^{-2})
$i_{am,n}$	the normal component of the electric current density at the SEI on the active-material domain side (A m^{-2})
$i_{e,n}$	the normal component of the electric current density at the SEI on the electrolyte side (A m^{-2})
K	rate coefficient (kmol m^{-2} s^{-1})
K_0	reference rate coefficient anode: 10^{-4} kmol m^{-2} s^{-1} [40] cathode: 10^{-8} kmol m^{-2} s^{-1} [40]
$\vec{n}_{am}$	normal vector at the SEI pointing outward from the active-material phase (−)
n_{am}	number of electrons that are involved in the electrode reaction at the SEI on the active-material domain side (−)
$\vec{n}_s$	normal vector at the SEI pointing outward from the electrolyte phase (−)
R	universal gas constant 8314.5 J kmol^{-1} K^{-1}
T	temperature (K)
t	time (s)
t_+^0	transference number (−) (Table 1)
U_{eq}	relative galvanic equilibrium potential of active material depending on state of charge of battery (V) (data is based on experimental data for a $LiCoO_2$ based Li-ion cathode by Karthikeyan et al.) [44]
α_1	electrode reaction order 0.5 [40]
α_2	vacancies reaction order 0.5 [40]
α_3	electrolyte reaction order 0.5 [40]
α_a	anodic transfer coefficient 0.5 [40]
α_c	cathodic transfer coefficient 0.5 [40]
η	kinetic overpotential (V)
κ	lithium ion conductivity (Ω^{-1} m^{-1}) (Table 1)
κ_d	variable to improve readability (A m^{-1})
σ	electrical conductivity anode: $10^6\ \Omega^{-1}$ m^{-1} (carbon) cathode current collector: $3.78 \times 10^7\ \Omega^{-1}$ m^{-1} (aluminium) active material: $1\ \Omega^{-1}$ m^{-1} [39] carbon-binder domain: $10^4\ \Omega^{-1}$ m^{-1} (assumed; notably lower than the conductivity of pure carbon at approximately $10^6\ \Omega^{-1}$ m^{-1})
ϕ	electrical potential (V)
$\Delta\phi$	electrical potential difference at the SEI; $\Delta\phi$ is calculated by subtracting the potential in the electrolyte from the potential in the active material at the point of interest (V)

The starting point of the work reported here is similar to Yan et al. [33] and Wiedemann et al. [34], where the two-phase reconstruction of a $LiCoO_2$ cathode based on X-ray nano-scale computer tomography (CT) images is combined with an electrochemical model. They introduced a new approach to model Li-ion batteries by employing a domain consisting of $LiCoO_2$ and electrolyte-filled pore space, which was directly derived from a tomographic method. Unlike them, our work is based on a three-phase reconstruction consisting of voxels characterised by their material properties as the active-material domain, carbon-binder domain or pore space. It has been shown that analysis based on a two-phase reconstruction which neglects the carbon-binder domain can produce appreciably different results compared to models based on a three-phase reconstruction [31]. In the reported work, we account for the carbon-binder domain and employ a three-phase reconstruction of the cathode which is included in a three-dimensional Li-ion battery model. It consists of a set of coupled nonlinear partial differential equations, which describe the potential and concentration distributions, comparable to the P2D model but without the assumption of macro-homogeneity.

2. Image processing and domain generation

A three-phase, three-dimensional reconstruction of a commercial $LiCoO_2$ Li-ion battery cathode based on recent work [30] is the starting point. It consists of 200 images with a spacing of 62 nm between images. Each image is composed of 572 × 518 square pixels with an edge length of 35 nm. The active-material domain, carbon-binder domain and pore space are depicted by voxels in three different colours (Fig. 1). The total reconstruction represents a volume of 20.02 μm × 18.13 μm × 12.4 μm.

The image stack was imported into Scilab [35] using the Scilab Image Processing Toolbox (SIP). To save calculation time, each image of the stack was resampled by a majority wins algorithm with the factor of 0.5. This results in images with a resolution of 286 × 259 pixels. Each pixel now has an edge length of 70 nm. Small irregularities that are due to mistakes during the segmentation process were removed by applying a self-implemented filter in Scilab. The filter replaces single voxels surrounded by voxels of a different phase along a spatial direction and adds these isolated voxels to the neighbouring phase. This filter was applied consecutively in each spatial direction. The post-processed image stack was imported into the software pro-STAR [36] to create a Cartesian type mesh, which was saved into a *.dbs file and finally entirely imported into STAR-CCM+ as a cathode [36].

The reconstruction process causes small pockets of electrolyte to occur within the carbon-binder phase. If considered, these regions would translate into mathematical null spaces in the linear system, leading to potential issues when solving the model. The same

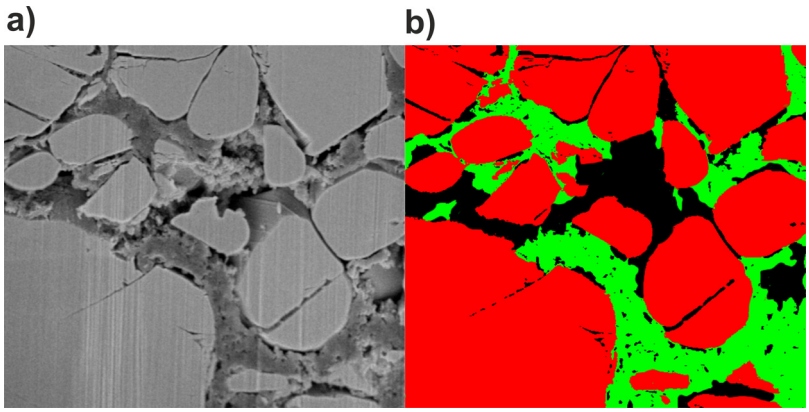

Fig. 1. The 3D representation [30] used to generate the cathode section of the model presented in this work was created by FIB/SEM imaging with successive segmentation steps. During segmentation, each voxel is identified as either belonging to pore space, the active-material domain or the carbon-binder domain. (a) One of the original aligned and cropped SEM images. (b) The same image after segmentation. The three phases are distinguishable by their respective colours (pore space—black, active-material domain—red, carbon-binder domain—green).

applies for small pieces of carbon binder immersed in electrolyte. These regions were removed using a Java macro within STAR-CCM+.

The result of all editing steps reduced the volume fraction of the electrolyte by 0.08% and the volume fraction of the carbon-binder domain by 0.22%. This is considered to have insignificant influence on the following simulation results.

To create a full electrochemical battery, a separator, a current collector consisting of aluminium on the cathode side and a carbon block representing the anode and anode current collector were added as single-phase regions (Fig. 2). The battery was meshed to form a three-dimensional domain consisting of approximately 21 million hexahedral cells. The porous structure of the separator is neglected. It is modelled as an electrolyte-filled region between the electrodes.

3. Model equations

Fundamentally, the three individual domains of the cathode differ from each other by their ability to transport lithium and electrons. In the investigations presented here, only electron transport is considered for the carbon-binder phase. Assuming the binder phase to be impermeable for the transport of lithium implies that no solid electrolyte interface can be formed at its boundary with the active material. By nature, the electrolyte phase is conductive only for lithium ions. The active-material domain conducts both lithium and electrons (Fig. 3).

The presented model is based on work by Doyle et al. [9] and Newman et al. [37]. The central equations are presented in the following section.

3.1. Electric potential

In all solid parts of the battery, the vector field describing the electric current density $\vec{\tau}$ at a given location is defined by Ohm's law

$$\vec{\tau} = \sigma \vec{E} \tag{1}$$

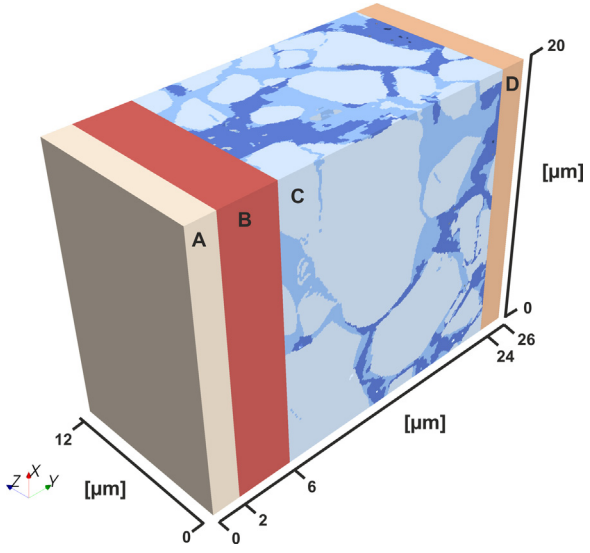

Fig. 2. The total calculation domain consisting of anode (A), separator (B), cathode (C) and cathode current collector (D). The *y* direction is the through-plane direction of the battery.

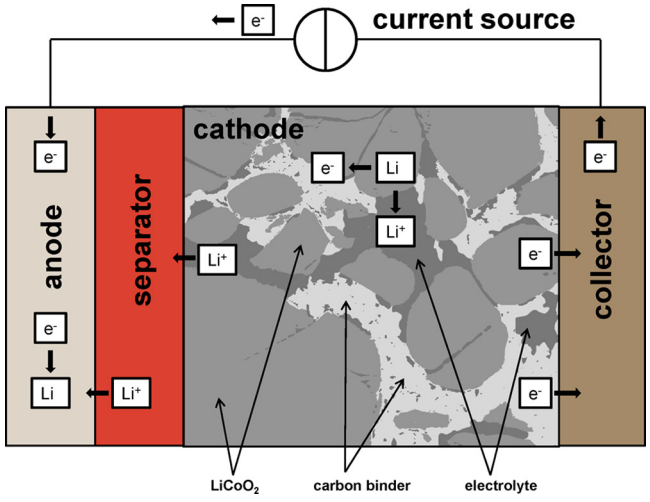

Fig. 3. The basic working principle of the model during charging of the battery. Lithium stored in the active-material domain is split into cations and electrons. The cations are transported through the electrolyte-filled pore space, across the separator and to the anode. Electrons are transported through the active-material domain (low conductivity) and the carbon-binder domain (high conductivity) to the cathode collector. The collector is electrically connected to the anode which allows recombination of cations and electrons at the anode. The relocation of lithium from the cathode to the anode, and thus the charging of the battery, is driven by an external current source.

with the material-specific electrical conductivity σ and the local value of the electric field $\vec{E}$. The electric field is expressed in terms of the negative gradient $\nabla$of the electric potential ϕ:

$$\vec{E} = -\nabla\phi \tag{2}$$

Within the pore space filled with electrolyte, the electric current density is not only governed by migration but also by diffusion and thus Ohm's law must be modified. The model assumes a $LiPF_6$ salt dissolved in a (1:1:1) volumetric mixture of EC:DMC:EMC solvents as an electrolyte. The current within the electrolyte is defined according to the approach of Doyle et al. [9,37,38], which is based on concentrated solution theory:

$$\vec{i} = \kappa\vec{E} + \kappa_d\nabla(\ln c_e) \tag{3}$$

where κ is defined as the ionic conductivity of the electrolyte, comparable to the electrical conductivity σ in all solid parts of the battery. The charge transfer within the electrolyte is accomplished by transferring lithium cations instead of electrons. The second term on the right-hand side adds the effect of diffusivity and is dependent on the lithium/salt concentration c_e and the variable κ_d. This variable is introduced to improve readability and is defined by

$$\kappa_d = \frac{2RT\kappa}{F}(1-t_+^0)\left[1+\frac{d(\ln f\pm)}{d(\ln c_e)}\right] \tag{4}$$

with the universal gas constant R, the temperature T, Faraday's constant F, the transference number t_+^0 of cations with respect to the velocity of the solvent species and the mean molar activity coefficient of the electrolyte $f_\pm$. Due to charge conservation, the electric current density field must be free of divergence:

$$\nabla\vec{i} = 0 \tag{5}$$

This finally yields the transport equations for the electric charge written in terms of the electric potential, cast in finite volume form:

$$\oint_S \kappa\nabla\phi ds - \oint_S \kappa_d\nabla(\ln c_e)ds = 0 \tag{6}$$

$$\oint_S \sigma\nabla\phi ds = 0 \tag{7}$$

Eq. (6) is valid within both the separator and the electrolyte phase; Eq. (7) is valid for all other components of the battery.

3.2. Concentration

A diffusion equation is solved for the lithium transport within the active-material domain

$$\frac{\partial}{\partial t}\int_V c_{am}dV = \oint_S D\nabla c_{am}ds \tag{8}$$

where c_{am} describes the molar concentration of lithium in the electrochemically active material domain and D is the material-specific, effective lithium diffusivity coefficient. Analogously to the equations for the electric potential, an additional term needs to be considered to account for migration within the electrolyte phase:

$$\frac{\partial}{\partial t}\int_V c_e\,dV = \oint_S D\nabla c_e\,ds - \int_V \frac{\vec{i}\cdot t_+^0}{F}\,dV \tag{9}$$

In the electrolyte, a concentrated solution correction to the salt diffusion coefficient D is applied:

$$D = D_0(1-\frac{d(\ln c_0)}{d(\ln c_e)}) \tag{10}$$

3.3. Solid electrolyte interface

The electric charge that is transferred across the interface between the electrolyte and the active-material domain, the so-called solid electrolyte interface (SEI), is conserved. Thus the absolute value of the normal components of the current density $\vec{i}$ on the active-material side ($i_{am,n}$) and the electrolyte side ($i_{e,n}$) must be equal. (In a conventional finite-volume context, the normal vector always points outward from the considered phase):

$$i_{am,n} = \vec{i}_{am}\cdot\vec{n}_{am} \tag{11}$$

$$i_{e,n} = \vec{i}_{e}\cdot\vec{n}_{e} \tag{12}$$

$$i_{am,n} = -i_{e,n} \tag{13}$$

Consequently, the potential interface conditions on the active-material side and the electrolyte side are defined as follows:

$$\left.\frac{\partial\phi}{\partial n_{am}}\right|_{SEI} = -\frac{i_{am,n}}{\sigma} \tag{14}$$

$$\left.\frac{\partial\phi}{\partial n_e}\right|_{SEI} = -\frac{\kappa_{e,n}}{\kappa} + \frac{\kappa_d}{\kappa}\frac{\partial(\ln c_e)}{\partial n_e} \tag{15}$$

Analogously, the flux of lithium across the SEI must be conserved and is described by

$$\left.\frac{\partial c_{am}}{\partial n_{am}}\right|_{SEI} = -\frac{i_{am,n}}{FD} \tag{16}$$

$$\left.\frac{\partial c_e}{\partial n_e}\right|_{SEI} = -\frac{i_{e,n}}{FD}(1-t_+^0) \tag{17}$$

The electric current density $i_{am,n} = -i_{e,n}$ that is transferred across the SEI is calculated using the Butler–Volmer equation, so that

$$i_{am,n} = i_0(e^{\frac{\alpha_a F\eta}{RT}} - e^{\frac{\alpha_c F\eta}{RT}}) + C\frac{\partial}{\partial t}(\Delta\phi) \tag{18}$$

with the specific double-layer capacitance C, the potential difference $\Delta\phi$ between the phases, the kinetic overpotential η, an anodic transfer coefficient α_a and a cathodic transfer coefficient α_c. The exchange current density i_0 is defined as

$$i_0 = FK\left(\frac{c_{am}}{c_{am,\max}}\right)^{\alpha_1}\left(1-\frac{c_{am}}{c_{am,\max}}\right)^{\alpha_2}\left(\frac{c_e}{c_{e,ref}}\right)^{\alpha_3} \tag{19}$$

where $c_{am,max}$ describes the molar concentration in a saturated active-material domain. Likewise c_e refers to the molar concentration of lithium ions in the electrolyte in relation to a reference concentration $c_{e,ref}$. α_1, α_2 and α_3 are the reaction orders for the electrode, the vacancies and the electrolyte, respectively. The SEI surface overpotential η is calculated by

$$\eta = \Delta\phi - U_{eq} - i_{am,n}R_{SEI} \tag{20}$$

with the relative galvanic equilibrium potential U_{eq} of the active-material domain. Both the rate coefficient K and the electrical resistance R_{SEI} of the SEI generally depend on the temperature:

$$K = K_0^{\frac{-E_a}{RT}} \tag{21}$$

$$R_{SEI} = R_0^{\frac{-E_{SEI}}{RT}} \tag{22}$$

where E_a is the kinetic activation energy, E_{SEI} the SEI activation energy.

The model does not account for the crystal structure of $LiCoO_2$. All the interfacial area between the active material and the electrolyte is assumed to be available for charge transfer. In reality,

Table 1
List of electrolyte parameters at 300 K as a function of lithium/salt concentration. The parameters were provided by K. Gering and are based on his advanced electrolyte model [40].

Lithium/salt concentration (kmol m^{-3})	Transference number (−)	Reference lithium diffusivity (m^2 s^{-1})	Lithium ion conductivity (Ω^{-1} m^{-1})	Concentrated solution correction to salt diffusivity (−)	Non-ideal solution correction to salt migration (−)
0.03	0.414	3.88E−10	0.07	−0.005	−0.13
0.06	0.415	3.79E−10	0.13	−0.005	−0.13
0.11	0.417	3.61E−10	0.26	−0.008	−0.09
0.17	0.419	3.44E−10	0.36	−0.012	−0.04
0.22	0.421	3.29E−10	0.46	−0.016	0.03
0.28	0.423	3.16E−10	0.55	−0.018	0.12
0.33	0.425	3.02E−10	0.63	−0.021	0.21
0.39	0.427	2.90E−10	0.70	−0.025	0.31
0.44	0.429	2.78E−10	0.77	−0.028	0.43
0.49	0.431	2.67E−10	0.83	−0.032	0.54
0.55	0.432	2.57E−10	0.88	−0.035	0.67
0.60	0.434	2.47E−10	0.93	−0.041	0.81
0.65	0.436	2.38E−10	0.97	−0.044	0.95
0.71	0.437	2.29E−10	1.01	−0.044	1.11
0.76	0.439	2.20E−10	1.04	−0.050	1.28
0.81	0.441	2.12E−10	1.06	−0.053	1.45
0.86	0.442	2.04E−10	1.09	−0.052	1.62
0.91	0.444	1.96E−10	1.10	−0.059	1.81
0.96	0.445	1.88E−10	1.12	−0.067	2.00
1.01	0.446	1.81E−10	1.13	−0.065	2.20
1.06	0.448	1.74E−10	1.13	−0.062	2.40
1.11	0.449	1.67E−10	1.13	−0.071	2.62
1.16	0.450	1.60E−10	1.13	−0.079	2.83
1.21	0.452	1.53E−10	1.13	−0.082	3.05
1.26	0.453	1.48E−10	1.12	−0.085	3.28
1.31	0.454	1.41E−10	1.11	−0.087	3.52
1.35	0.455	1.35E−10	1.10	−0.089	3.78
1.40	0.456	1.29E−10	1.09	−0.092	4.00
1.45	0.457	1.24E−10	1.07	−0.096	4.22
1.50	0.458	1.18E−10	1.06	−0.098	4.46
1.54	0.459	1.13E−10	1.04	−0.101	4.71
1.59	0.460	1.08E−10	1.02	−0.103	4.97
1.64	0.461	1.03E−10	1.00	−0.105	5.24
1.68	0.462	9.88E−11	0.98	−0.108	5.49
1.73	0.463	9.43E−11	0.95	−0.120	5.73
1.77	0.464	8.98E−11	0.93	−0.132	6.02
1.82	0.465	8.59E−11	0.91	−0.124	6.31
1.86	0.466	8.19E−11	0.88	−0.117	6.51
1.91	0.467	7.81E−11	0.86	−0.130	6.71
1.95	0.468	7.46E−11	0.84	−0.143	6.99
2.00	0.469	7.12E−11	0.81	−0.134	7.33
2.04	0.470	6.78E−11	0.79	−0.137	7.65
2.08	0.471	6.46E−11	0.76	−0.151	7.95
2.13	0.472	6.15E−11	0.74	−0.140	8.28
2.17	0.472	5.84E−11	0.71	−0.143	8.58
2.21	0.473	5.55E−11	0.69	−0.159	8.89
2.25	0.474	5.28E−11	0.66	−0.161	9.24
2.30	0.475	5.01E−11	0.64	−0.163	9.59
2.34	0.476	4.75E−11	0.62	−0.166	9.95
2.38	0.477	4.50E−11	0.59	−0.141	7.96
2.42	0.478	4.27E−11	0.57	−0.141	7.96

the $LiCoO_2$ crystal consists of layers and lithium can only penetrate through the openings between the layers. Further, the layered structure of $LiCoO_2$ results in an anisotropic diffusivity, and electrical conductivity [39]. Finally, the particles can change shape due to changes in the lithium content. The importance of these effects is hard to gauge as the underlying crystal structure of the $LiCoO_2$ particles, as oriented in the electrode structure, has yet to be characterized.

The model was implemented in STAR-CCM+ [36]. Although the implementation would allow the computation of a thermal solution, the temperature is fixed at 300 K to reduce calculation time. The electrolyte transport and thermodynamic parameters used to demonstrate the feasibility of the model were provided by K. Gering and are based on his advanced electrolyte model [40]. The remaining parameters are either taken from literature or when not available assumed. All parameters are presented in the *List of symbols* and in Table 1.

4. Results and discussion

To demonstrate feasibility, we simulate a 1 C charge process. The nominal cell capacity was computed to be 7.945×10^{-6} A s, based on cut-off cell potential values of 3.6 and 4.2 V. A Neumann boundary condition of 8.89 A m^{-2} is applied at the outer faces of the anode and the cathode current collector. A Dirichlet point for the electric potential was set within the domain to guarantee a unique solution of the electric potential. The solution time was 27 days on a cluster consisting of single nodes with two Intel Xeon E5-2680 CPUs and 32 GB RAM each. Up to four nodes were used for calculation.

During the charging process, both open-circuit and closed-circuit cell potential are monitored as a function of the state of charge (SOC) (Fig. 4). The difference between the cell potential curves, which describes the potential drop across the battery, is observed to remain at an approximately constant value of 100 mV. A detailed investigation of simulation data showed that roughly one

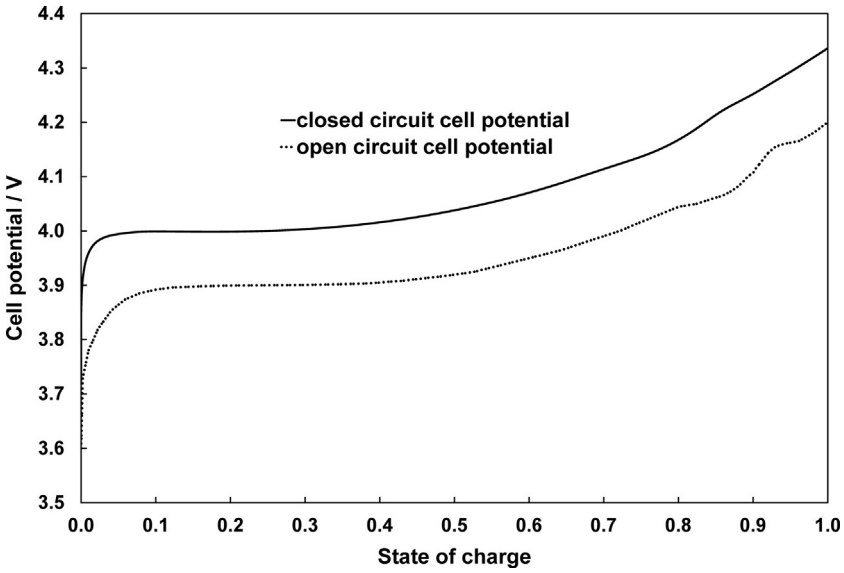

Fig. 4. Closed-circuit and open-circuit cell potential versus state of charge during charging of the battery. The difference between the two cell potential curves stays at an approximately constant value of 0.1 V.

half of this potential drop can be attributed to kinetic overpotential and one half to losses in the electrolyte (~50 mV). The electric potential drop in the carbon-binder phase was found to be negligible. Taking into account that the studied sample represents roughly a quarter of the thickness of a commercial cathode, the potential drop within the electrolyte can be estimated to be four times higher across a full cell (~200 mV). With the kinetic overpotential, which is not influenced directly by the thickness of the electrode, the resulting magnitude of a predicted electric potential drop for the full cell (~250 mV) is therefore only slightly higher than experimentally observed potential drops for commercial 18,650 cells [41]. This deviation can be explained by the low volume fraction for the electrolyte of 0.13, which was derived from the tomographic method applied [30,31].

4.1. Active material domain

In models that only resolve active-material and electrolyte phases, the lack of the carbon binder as the electric conductor needs to be compensated by assigning a considerably higher value of electric conductivity to the active-material domain, to obtain results in agreement with experimental measurements. The introduction of a carbon-binder domain into the model allows realistic values of active-material electric conductivity to be used, as obtained by experimental measurement of the bulk material.

An additional effect, introduced by explicitly modelling the carbon-binder phase, manifests itself as a reduced available SEI surface to volume ratio, when compared to a corresponding two-phase configuration modelling only the active material and electrolyte. If the carbon-binder phase were removed from the 3D reconstruction employed in this study, the modelled SEI surface to volume ratio would increase by 72% from 6.5×10^5 to 11.2×10^5 m^2 m^{-3}. It is evident that including the carbon-binder phase in simulations is crucial in order to realistically reproduce the physically existent SEI surface area within the simulation.

When studying the distribution of lithium concentration in the active-material domain during the simulated charge process, we observe that all $LiCoO_2$ grains expel lithium (Fig. 5). However, the discharge and the resulting concentration in the grains are not homogeneous, which is partly due to coverage by the carbon binder and partly due to the size and position of the active-material domains. This can be explained by regarding the following cases (Fig. 6):

(1) The smaller the active-material grain, the more likely it will release lithium into the electrolyte. This leads to a lower average lithium concentration in smaller grains. This can be explained

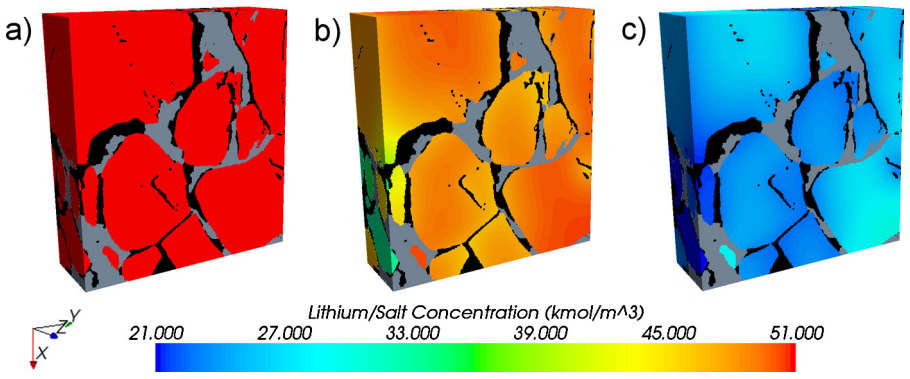

Fig. 5. Cross-sections of the cathode at various states of charge depicting the respective lithium/salt concentration in the active-material domain (Electrolyte-black, carbon-binder domain-dark grey). (a) SOC 0 (initial state). (b) SOC 0.1. (c) SOC 1 (fully charged).

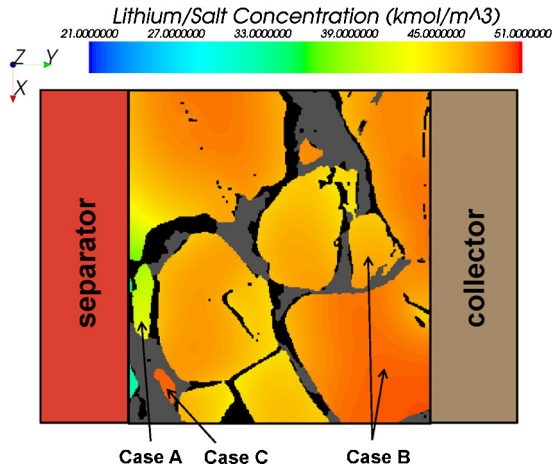

Fig. 6. Cross-section of the cathode at state of charge 0.15, depicting the lithium/salt concentration in the active-material domain (Electrolyte-black, carbon-binder domain-dark grey). Three different cases explain gradients in the lithium/salt concentration of the active-material domain during charging. *Case A:* Small active-material particles near the separator display the lowest lithium/salt concentration. They are most likely to release lithium due to short diffusion and migration lengths in both the particle itself and the electrolyte-filled pore space. *Case B:* Even though both particles are situated at a similar distance from the separator and thus the anode, the larger particle displays a higher average lithium/salt concentration. This is due to the longer diffusion length of lithium situated in the middle of the larger particle to the SEI. *Case C:* Even though this active-material particle is very close to the separator, its lithium/salt concentration is relatively high. This is due to limited access to the electrolyte as a result of nearly complete coverage by carbon binder. This hinders the transport of lithium out of the particle.

by a shorter average distance to the SEI for the lithium in the active-material grains (Fig. 6; Case A).

(2) The further the active-material grain is away from the separator, the less likely it is to release lithium into the electrolyte. This leads to higher average lithium concentration in these grains. This can be explained by longer diffusion and migration paths from the SEI to the anode (Fig. 6; Case B).

(3) The effects mentioned in 1 and 2 superimpose each other. Small, active-material grains near the separator display the lowest lithium concentration, large grains near the cathode current collector the largest.

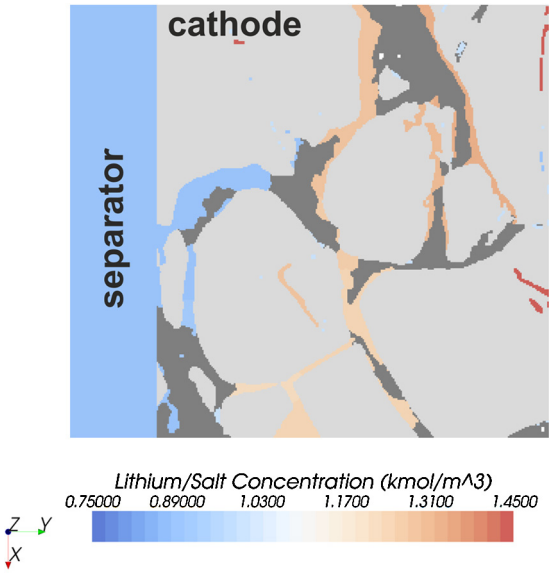

Fig. 8. Cross-section of the cathode and separator that illustrates how the lithium/salt concentration is distributed in the electrolyte (carbon-binder domain-dark grey, active-material domain-light grey). The further the electrolyte-filled pore space is away from the anode, the higher the concentration. The battery is fully charged.

(4) If the surface area and thus the SEI of an active-material grain is mostly covered by carbon binder, this considerably hinders lithium transfer to the electrolyte. These grains consequently display a relatively high average lithium concentration (Fig. 6; Case C).

4.2. Electrolyte phase

When plotting the lithium/salt concentration in the electrolyte during the simulated charging process, we observe a considerable difference between minimum and maximum values (Fig. 7). In an uncharged state – which represents the initial condition of the simulation – the electrolyte displays an average lithium/salt concentration of 1 kmol m^{-3}. After charging starts, the concentration is quickly redistributed to the range between approximately 0.9 and

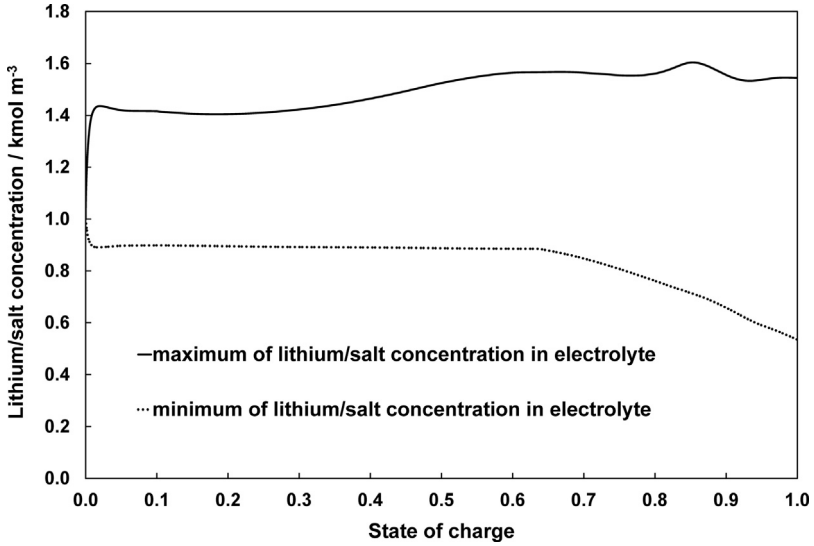

Fig. 7. Maximum and minimum of lithium/salt concentration in the electrolyte. This is significant because the parameter influences the ability of the electrolyte to transport lithium cations (Table 1) and thus the performance of the battery.

1.5 kmol m^{-3}. At a SOC of 0.02, which corresponds to 72 s in physical time, the lithium/salt concentration apparently approaches a quasi-steady state regime, exhibiting almost constant values. In the SOC range between 0.65 and 1, the minimum lithium/salt concentration further decreases to a value of 0.5 kmol m^{-3}, which can be attributed to very small regions in the electrolyte where starvation occurs. This effect is seen to be of very limited significance for the globally observed cell behaviour.

Regarding the spatial lithium/salt distribution in the cathode electrolyte (Fig. 8), the lowest concentration occurs near the separator. The concentration increases with distance from the separator. The observed strong non-uniformity in the lithium/salt distribution is highly relevant for battery cell performance: The electrochemical parameters describing the electrolyte are strongly dependent on the lithium/salt concentration [42].

5. Conclusion

In this study, a three-dimensional finite volume model for Li-ion batteries featuring anode, cathode, current collectors and separator was introduced. The cathode is a spatially resolved three-phase domain based on FIB/SEM reconstruction. The three phases are active material, carbon binder and electrolyte-filled pore space. To demonstrate feasibility, a 1 C charge process was simulated. While previous models commonly compensate the role of the carbon-binder domain as an electric conductor by simply increasing the electric conductivity of the active-material phase, this work considers realistic conductivity values for all phases.

Results show that including a spatially resolved carbon-binder phase in the simulation is necessary to achieve more realistic battery models. We observe that partial coverage of active-material grain surface by carbon binder ensures excellent transport of electrons to and away from reaction centres, but adversely blocks part of the SEI, reducing the total available surface area between active-material grains and electrolyte. This subsequently leads to higher transport losses, effectively decreasing the system efficiency. Optimizing coverage could be an item for future battery design studies.

Additionally, we determined that considerable gradients of lithium/salt concentration form during battery charging. This leads to non-optimal transport parameters in the cathode near the separator and the current collector.

Acknowledgements

We thank the following colleagues for their support and fruitful discussions: Boris Kaludercic, Samir Muzaferija and Milovan Peric.

References

[1] V. Ramadesigan, P.W.C. Northrop, S. De, S. Santhanagopalan, R.D. Braatz, V.R. Subramanian, Modeling and simulation of lithium-ion batteries from a systems engineering perspective, Journal of the Electrochemical Society 159 (2012) R31.
[2] D. Zhang, B.N. Popov, R.E. White, Modeling lithium intercalation of a single spinel particle under potentiodynamic control, Journal of the Electrochemical Society 147 (2000) 831.
[3] S. Santhanagopalan, Q.Z. Guo, P. Ramadass, R.E. White, Review of models for predicting the cycling performance of lithium ion batteries, Journal of Power Sources 156 (2006) 620.
[4] M. Guo, G. Sikha, R.E. White, Single-particle model for a lithium-ion cell: thermal behaviour, Journal of The Electrochemical Society 158 (2011) A122.
[5] J. Newman, W. Tiedemann, Porous-electrode theory with battery applications, AIChE Journal 21 (1975) 25.
[6] G.G. Botte, V.R. Subramanian, R.E. White, Mathematical modeling of secondary lithium batteries, Electrochimica Acta 45 (2000) 2595.
[7] P.M. Gomadam, J.W. Weidner, R.A. Dougal, R.E. White, Mathematical modeling of lithium-ion and nickel battery systems, Journal of Power Sources 110 (2002) 267.
[8] M. Doyle, J. Newman, A.S. Gozdz, C.N. Schmutz, J.M. Tarascon, Comparison of modeling predictions with experimental data from plastic lithium ion cells, Journal of The Electrochemical Society 143 (1996) 1890.
[9] M. Doyle, T.F. Fuller, J. Newman, Modeling of galvanostatic charge and discharge of the lithium/polymer/insertion cell, Journal of The Electrochemical Society 140 (1993) 1526.
[10] P. Arora, M. Doyle, A.S. Gozdz, R.E. White, J. Newman, Comparison between computer simulations and experimental data for high-rate discharges of plastic lithium-ion batteries, Journal of Power Sources 88 (2000) 219.
[11] T.F. Fuller, M. Doyle, J. Newman, Simulation and optimization of the dual lithium ion insertion cell, Journal of The Electrochemical Society 141 (1994) 1.
[12] G. Ning, R.E. White, B.N. Popov, A generalized cycle life model of rechargeable Li-ion batteries, Electrochimica Acta 51 (2006) 2012.
[13] P. Ramadass, B. Haran, P.M. Gomadam, R. White, B.N. Popov, Development of first principles capacity fade model for Li-ion cells, Journal of The Electrochemical Society 151 (2004) A196.
[14] P. Ramadass, B. Haran, R. White, B.N. Popov, Mathematical modeling of the capacity fade of Li-ion cells, Journal of Power Sources 123 (2003) 230.
[15] V. Srinivasan, C.Y. Wang, Analysis of electrochemical and thermal behavior of Li-ion cells, Journal of The Electrochemical Society 150 (2003), A98.
[16] J.R. Wilson, J.S. Cronin, S.A. Barnett, S.J. Harris, Measurement of three-dimensional microstructure in a $LiCoO_2$ positive electrode, Journal of Power Sources 196 (2011) 3443.
[17] R.N. Methekar, K. Chen, R.D. Braatz, V.R. Subramanian, Kinetic Monte Carlo simulation of surface heterogeneity in graphite electrodes for lithium-ion batteries: Passive layer formation, Journal of The Electrochemical Society 158 (2011) A363–A370.
[18] R.M. Spotnitz, B. Kaludercic, S. Muzaferija, M. Peric, G. Damblanc, S. Hartridge, Geometry-resolved electro-chemistry model of Li-ion batteries, SAE International Journal of Alternative Powertrains 1 (2012) 160.
[19] R.E. Garcia, Y.M. Chiang, W.C. Carter, P. Limthongkul, C.M. Bishop, Microstructural modeling and design of rechargeable lithium-ion batteries, Journal of The Electrochemical Society 152 (2005) A255.
[20] C.W. Wang, A.M. Sastry, Mesoscale modelling of a li-ion polymer cell, Journal of The Electrochemical Society 154 (2007) A1035.
[21] J.P. Meyers, M. Doyle, R.M. Darling, J. Newman, The impedance response of a porous electrode composed of intercalation particles, Journal of The Electrochemical Society 147 (2000) 2930.
[22] D.E. Stephenson, E.M. Hartman, J.N. Harb, D.R. Wheeler, Modeling of particle-particle interactions in porous cathodes for lithium-ion batteries, Journal of The Electrochemical Society 154 (2007) A1146.
[23] G.S. Nagarajan, J.W. Van Zee, R.M. Spotnitz, A mathematical model for intercalation electrode behavior. I. Effect of particle-size distribution on discharge capacity, Journal of The Electrochemical Society 145 (1998) 771.
[24] L. Holzer, F. Indutnyi, P.H. Gasser, B. Münch, M. Wegmann, Three-dimensional analysis of porous $BaTiO_3$ ceramics using FIB nanotomography, Journal of Microscopy 216 (2004) 84.
[25] T. Hutzenlaub, J. Becker, R. Zengerle, S. Thiele, How coarsening the 3D reconstruction of a porous material influences diffusivity and conductivity values, ECS Electrochemistry Letters 2 (2013) F14.
[26] T. Hutzenlaub, J. Becker, R. Zengerle, S. Thiele, Modelling the water distribution within a hydrophilic and hydrophobic 3D reconstructed cathode catalyst layer of a proton exchange membrane fuel cell, Journal of Power Sources 227 (2013) 260.
[27] J.R. Wilson, W. Kobsiriphat, R. Mendoza, H.Y. Chen, J.M. Hiller, D.J. Miller, K. Thornton, P.W. Voorhees, S.B. Adler, S.A. Barnett, Three-dimensional reconstruction of a solid-oxide fuel-cell anode, Nature Materials 5 (2006) 541.
[28] C. Ziegler, S. Thiele, R. Zengerle, Direct three-dimensional reconstruction of a nanoporous catalyst layer for a polymer electrolyte fuel cell, Journal of Power Sources 196 (2011) 2094.
[29] S. Thiele, R. Zengerle, C. Ziegler, Nano-morphology of a polymer electrolyte fuel cell catalyst layer - imaging, reconstruction and analysis, Nano Research 4 (2011) 849.
[30] T. Hutzenlaub, S. Thiele, R. Zengerle, C. Ziegler, Three-dimensional reconstruction of a $LiCoO_2$ Li-ion battery cathode, Electrochemical and Solid-State Letters 15 (2012) A33.
[31] T. Hutzenlaub, A. Asthana, J. Becker, D.R. Wheeler, R. Zengerle, S. Thiele, FIB/SEM-based calculation of tortuosity in a porous $LiCoO_2$ cathode for a Li-ion battery, Electrochemistry Communications 27 (2013) 77.
[32] M. Ender, J. Joos, T. Carraro, E. Ivers-Tiffée, Three-dimensional reconstruction of a composite cathode for lithium-ion cells, Electrochemistry Communications 13 (2011) 166.
[33] B. Yan, C. Lim, L. Yin, L. Zhu, Three dimensional simulation of galvanostatic discharge of $LiCoO_2$ cathode based on x-ray nano-CT images, Journal of The Electrochemical Society 159 (2012) A1604.
[34] A.H. Wiedemann, G.M. Goldin, S.A. Barnett, H. Zhu, R.J. Kee, Effects of three-dimensional cathode microstructure on the performance of lithium-ion battery cathodes, Electrochimica Acta 88 (2013) 580.
[35] www.scilab.org, 2013.
[36] www.cd-adapco.com, 2013.
[37] J. Newman, K.E. Thomas-Alyea, Electrochemical Systems, Wiley, Hoboken, NJ, 2004.
[38] M. Doyle, T.F. Fuller, J. Newman, The importance of the lithium ion transference number in lithium/polymer cells, Electrochimica Acta 39 (1994) 2073.
[39] Y. Takahashi, Y. Gotoh, J. Akimoto, S. Mizuta, K. Tokiwa, T. Watanabe, Anisotropic electrical conductivity in $LiCoO_2$ single crystal, Journal of Solid State Chemistry 164 (2002) 1.

[40] K.L. Gering, Prediction of electrolyte viscosity for aqueous and non-aqueous systems: Results from a molecular model based on ion solvation and a chemical physics framework, Electrochimica Acta 51 (2006) 3125.
[41] J. Fan, On the discharge capability and its limiting factors of commercial 18650 Li-ion cell at low temperatures, Journal of Power Sources 117 (2003) 170.
[42] L.O. Valøen, J.N. Reimers, Transport properties of $LiPF_6$-based Li-ion battery electrolytes, Journal of The Electrochemical Society 152 (2005), A882.
[43] Y.I. Jang, B.J. Neudecker, N.J. Dudney, Lithium diffusion in Li_xCoO_2 ($0.45 < x < 0.7$) intercalation cathodes, Electrochemical and Solid-State Letters 4 (2001) A74.
[44] D.K. Karthikeyan, G. Sikha, R.E. White, Thermodynamic model development for lithium intercalation electrodes, Journal of Power Sources 185 (2008) 1398.